Supporting Information

Interrupted Chemical Reaction-based Tri-Phase Design of the $FeMoO_4/CuFe_2S_3/CuSe_2$ Electrocatalyst for Enhancing Electrochemical Nitrogen Reduction

Meselu Eskezia Ayalew[a], Abambagade Abera Mitiku[a], Tsegaye Girma Eshetu[b], Quoc-Nam Ha[a], Van-Nho Tran[a], Li-Duan Tsai,[c] Yin-Wen Tsai,[c] and Dong-Hau Kuo[a, b]*

[a] Department of Materials Science and Engineering, National Taiwan University of Science and Technology, No. 43, Section 4, Keelung Road, Taipei 106335, Taiwan

[b] Graduate Institute of Energy and Sustainability Technology, National Taiwan University of Science and Technology, No.43, Section 4, Keelung Road, Taipei 106335, Taiwan

[c] Material and Chemical Research Laboratories, Industrial Technology Research Institute, Chutung, Hsinchu 31041, Taiwan

*Corresponding author

E-mail: dhkuo@mail.ntust.edu.tw; Fax: +011-886-2-27303291

Table S1. Molar content of each precursor chemical for preparing the electrochemical catalysts

No	Catalyst code	$Fe(NO_3)_3 \cdot 9H_2O$)	$Cu(NO_3)_3$	$(NH_4)_5Mo_7O_{24} \cdot 4H_2O$)	Catalyst load (mg)	Foam size (cm^2)
1	FeCu (2:2)	2	2	0	2.65	1x1
2	MoCu (3:2)	0	2	3	2.8	1x1
3	FeMo (2:3)	4	0	6	3.7	1x1
4	FeMoCuSe (2:3:2:0)	2	3	2	2.3	1x1
5	FeMoCuSe(2:3:2:0.7)	2	3	2	4.7	1x1
6	FeMoCuSe(2:3:2:1.4)	2	3	2	4.51	1x1
7	FeMoCuSe(2:3:2:2.1)	2	3	2	5.01	1x1

Note: During catalyst labeling, the elemental symbols indicate precursor metal type, and the number shows the ratio (in mmol) used during mixing.

1. Quantification of nitrate, nitrite, and hydrazine using colorimetric analyses

1.1. Procedure for nitrate (NO_3^-) detection

For nitrate determination, 2 mL of the diluted electrolyte was mixed thoroughly with 100 µL of 1 M HCl, 10 µL of a 0.8 wt.% sulfamic acid solution, and 2 mL of deionized water. After allowing the mixture to react for 20 minutes, the absorbance at 220 and 275 nm was recorded using UV–visible spectroscopy. The final absorbance value was calculated using the equation $A = A_{220} - 2A_{275}$, and the nitrate (NO_3^-) concentration was determined from a calibration curve.

1.2. Detection and analysis of nitrite (NO_2^-)

Nitrite was quantified using the Griess reagent method[1]. The Griess reagent was prepared by dissolving 0.1 g of N-(1-naphthyl)ethylenediamine dihydrochloride, 1.0 g of sulfanilamide, and 2.94 mL of H_3PO_4 in 50 mL of deionized water. For analysis, 2 mL of the diluted electrolyte was mixed with 1 mL of Griess reagent and 2 mL of deionized water, then incubated for 15 minutes. The absorbance was then measured at 540 nm using a UV–visible spectrophotometer, and the

nitrite (NO_2^-) concentration was determined from a calibration curve [1, 2].

1.3. Procedure for hydrazine (N_2H_4) determination

The by-product N_2H_4 was determined using the method of Watt and Chrisp[3]. To determine hydrazine (N_2H_4) production, 150 mL of ethanol was combined with 15 mL of 37 wt.% HCl and 3 g of p-(dimethylamino)benzaldehyde to prepare the detection solution. Then, 1.5 mL of the test electrolyte was mixed with 1.5 mL of this solution. After 20 minutes of reaction, the absorbance of the mixture was measured at 460 nm using UV–visible spectroscopy, and the hydrazine concentration was calculated from a standard calibration curve.

1.4. Procedure for ^{1}H NMR characterization

Before the nitrogen reduction reaction (N_2RR), the electrolyte was purged with high-purity Ar for 30 minutes to remove residual gas. Subsequently, $^{15}N_2$ bubbled through the electrolyte for 20 minutes. Electrolysis was then performed for 1 hour at −0.6 V versus RHE in 0.5 M Na_2SO_4. The resulting $^{15}NH_4^+$-containing 600 μL electrolyte was concentrated and mixed with D_2O and DMSO-d6 prior to ^{1}H NMR measurement. The same procedure was followed for a sample prepared with $^{14}N_2$ as the feed gas.

2. Outcomes of the control experiments

The credibility of N_2RR experiments depends strongly on carefully designed control tests. To rule out ammonia contamination from the H-cell, electrodes, and Nafion 211 membrane, which can act as both sources and sinks of NH_3 during N_2RR, all components were thoroughly cleaned before experimentation. XRD, XPS, and SEM-EDS analyses confirmed that no nitrogen species were present in the as-prepared catalysts, even though nitrogen-containing precursors were used during synthesis. Additional control experiments were conducted to further verify that the detected NH_3

originated exclusively from the supplied N_2, and the corresponding results are discussed below.

a) When Ar was used as the feed gas in the Ar-saturated experiment, no NH_3 was detected, indicating the absence of residual nitrogen from either the feed gas or the components of the H-type electrolytic cell. This result confirms that, even under suitable electrolysis conditions, NH_3 cannot be produced without a nitrogen source, underscoring the essential role of N_2 in ammonia formation.

b) Electrolyte samples were collected from both the cathodic and anodic compartments to assess potential NH_3 crossover. No NH_3 was detected in the anodic chamber, confirming that ammonia generated at the cathode does not migrate through the membrane in the H-type cell. The Nafion 211 membrane, acting as a proton exchange membrane (PEM), enables selective proton (H^+) transport from the anode to the cathode while effectively separating the anodic and cathodic products. This separation prevents NH_3 crossover and avoids direct gas mixing between the two compartments.

c) When the Nafion 211 membrane was removed, only a negligible NH_3 yield was observed. In the absence of the membrane, direct contact and mixing between the anodic and cathodic compartments occur, allowing NH_3 generated at the cathode during N_2RR to be readily oxidized at the anode. This leads to an underestimation of the actual NH_3 yield and introduces measurement interference. These results underscore the critical role of a membrane-separated reactor configuration in N_2RR, as it suppresses NH_3 oxidation and ensures reliable quantification. Accordingly, this study emphasizes that electrochemical NH_3 synthesis should be carried out in an H-type cell equipped with a separating membrane. These critical control experiments confirm that the detected NH_3 originates from the electrochemical reduction of feed N_2 using the as-prepared catalyst.

3. Faradaic Efficiency, Energy Efficiency, and Energy Consumption Calculation

The Faradaic efficiency (FE) of the N_2RR was determined according to Equation (1):

$$\%FE = \frac{3 \times F \times C_{NH4+} \times V(mL)}{17 \times Q} \quad \text{..... (1)}$$

$$\%FE = \frac{3 \times \frac{96500\ C}{mol} \times 136\ \frac{\mu g}{mL} \times 90\ mL}{17 \times 222.14\ A/s} \times 100 = 93.8\%$$

Here, C_{NH4^+} (136 μg/mL) represents the concentration of generated ammonium ions, V (90mL) is the volume of 0.5 M Na_2SO_4 in the cathode chamber, F is the Faraday constant (96,500 C/mol), and Q denotes the total charge passed during the N_2RR, obtained from the chronoamperometry (CA) curve using an effective sample area of 1×1 cm^2. This Faradaic efficiency is a record high.

To evaluate the energy efficiency (EE) of ammonia electrosynthesis relative to the conventional Haber–Bosch process, the specific energy consumption (EC) was calculated in units of kWh per kg of NH_3 produced. This was done using the following equation, which allows a direct comparison of the energy demands between the two methods.

$$EC = \frac{n \times F \times V_{cell}}{3600 \times FE \times M} \quad \text{.....(2)}$$

$$EC = \frac{n \times F \times V_{cell}}{3600 \times FE \times M} = \frac{3 \times 96500 \times 2.0}{3600 \times 50.9 \times 17} = \frac{579000}{3115080} = 18.58\ kWh/kgNH3$$

Here n denotes the number of electrons transferred per mole of ammonia produced ($3e^-$), F is the Faraday constant (96,500 C/mol), V_{cell} represents the applied cell voltage (2.0 V), FE is the Faradaic efficiency (50.9%), and M is the molecular weight of NH_3(17 g/mol). For calculating energy consumption, an optimized cell voltage of 2.0 V was used to maximize ammonia

production. The electrocatalytic energy efficiency (EE) of the single-stack cell was then evaluated based on this calculation using the corresponding equation.

$$EE(\%) = \frac{(1.23 - E^{o}) \times FE}{E} \quad \text{.....(3)}$$

$$EE(\%) = \frac{(1.23 - 0.092) \times 50.9}{2.0} = \frac{57.92}{2} = 28.96$$

where E^0 is the standard potential of N_2RR to NH_3, which is 0.092 V *vs.* RHE; FE is the faradaic efficiency for ammonia, which is 50.9%; E or E_{cell} is the applied potential, which is 2.0 V; F is the Faraday constant (96 500 C mol^{-1}).

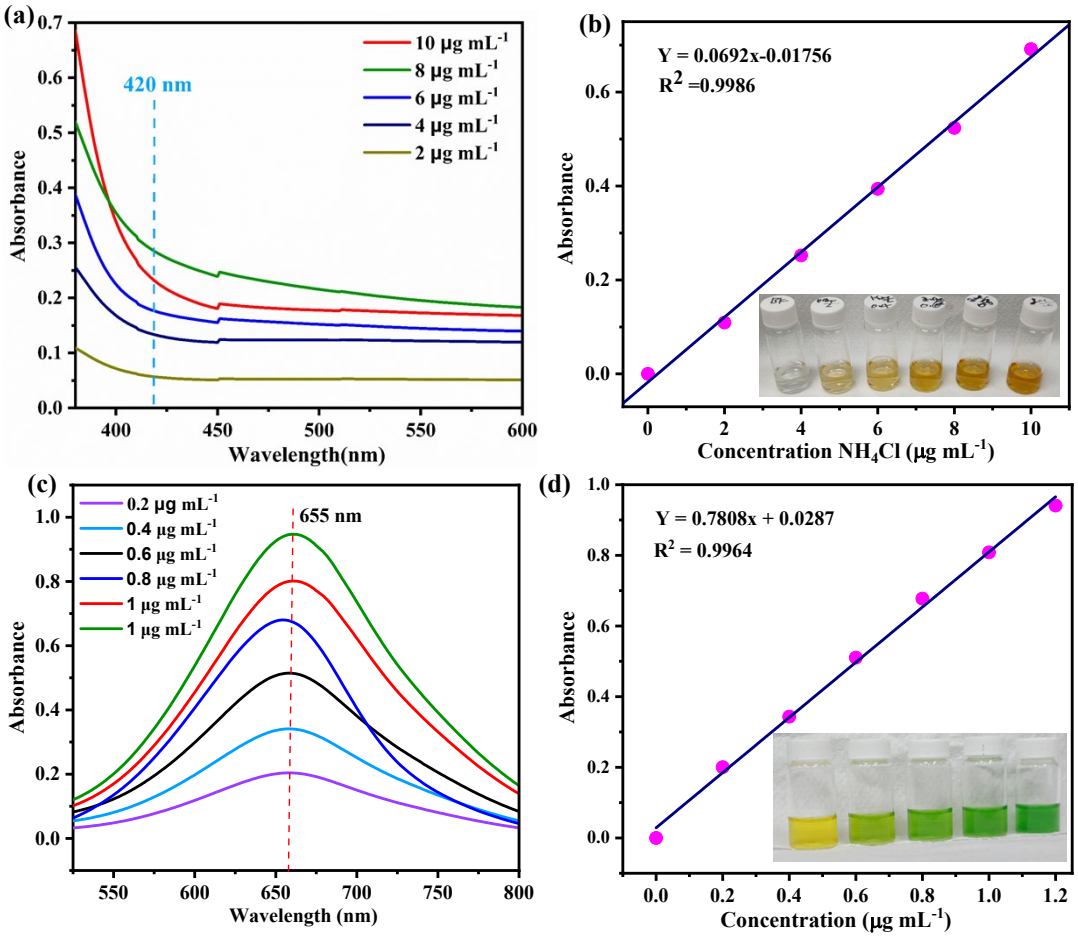

Figure S1. (a) The calibration curve at 420 nm is used to determine the NH_3 concentration. (b) UV-vis adsorption curves at different ammonium chloride concentrations, as measured by the

Nessler method, are used for calibration. (c) The calibration curve at 655 nm is used to determine the NH_3 concentration. (d) UV-vis adsorption curves at different ammonium chloride concentrations.

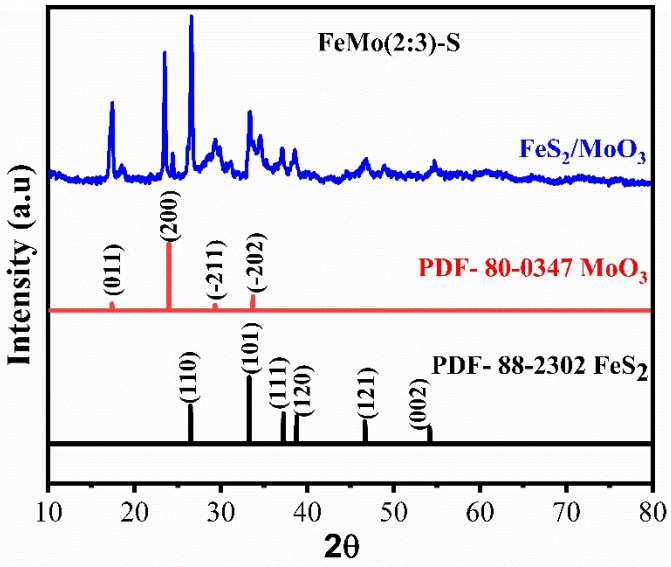

Figure S2. XRD patterns of FeS_2 and MoO_3 phases from the FeMo (2:3) bimetals system.

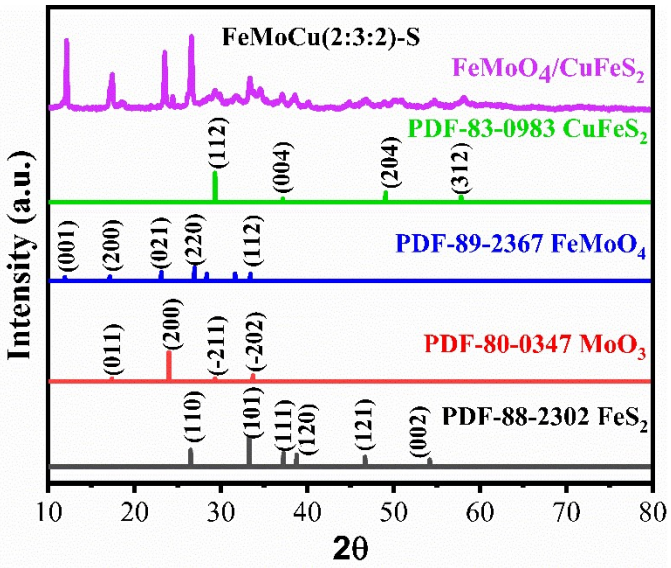

Figure S3. XRD patterns of $FeMoO_4$ and $CuFeS_2$ phases from the FeMoCu(2:3:2) system.

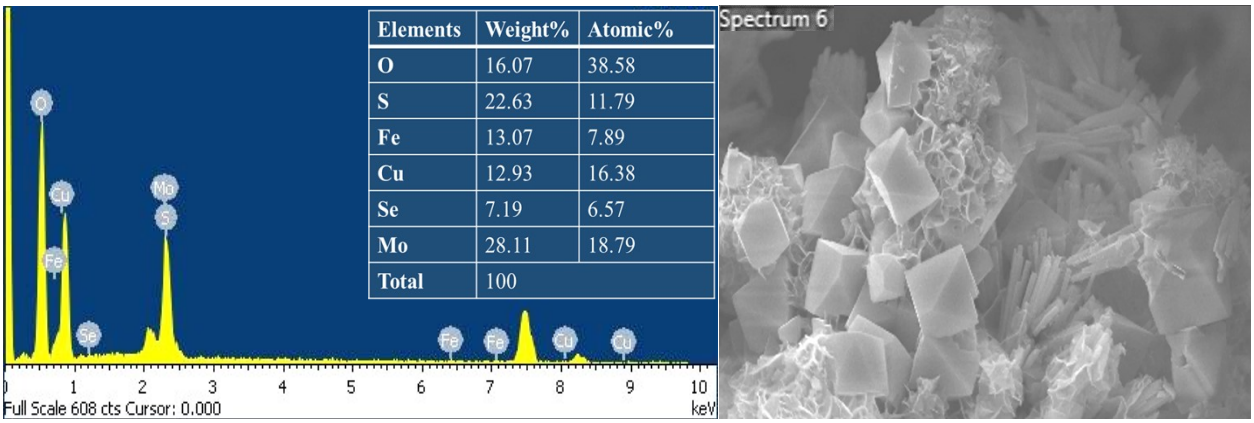

Figure S4. Large-area SEM-EDS compositional analysis of the $FeMoO_4/CuFe_2S_3/CuSe_2$ catalyst.

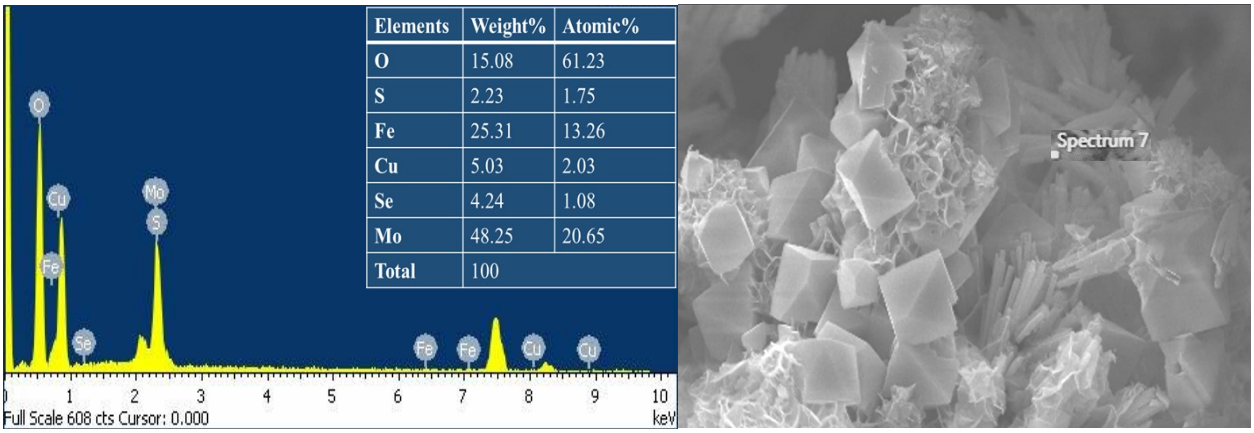

Figure S5. Small-area SEM-EDS compositional analysis of the $FeMoO_4$ phase in the $FeMoO_4/CuFe_2S_3/CuSe_2$ catalyst.

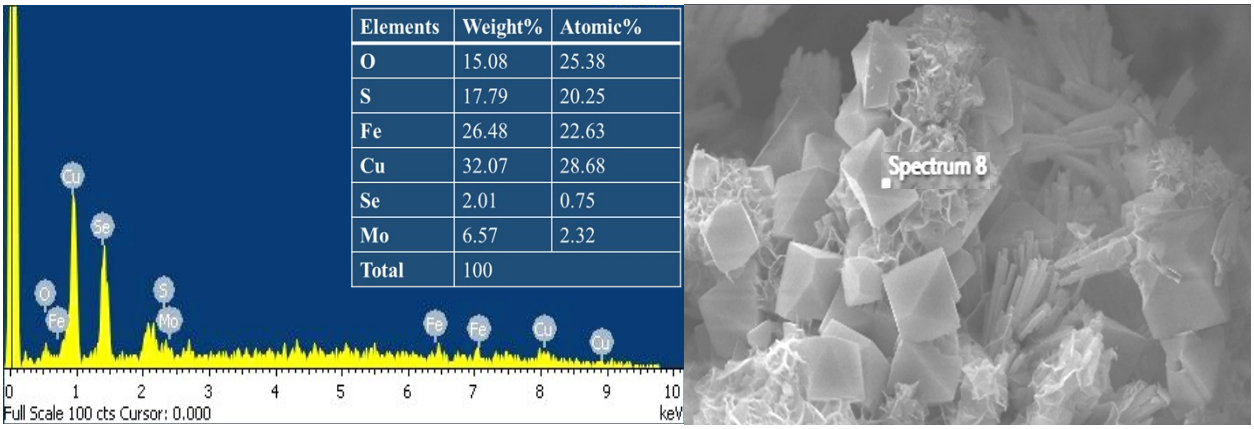

Figure S6. Small-area SEM-EDS compositional analyses of the $CuFe_2S_3$ phase in the the $FeMoO_4/CuFe_2S_3/CuSe_2$ catalyst.

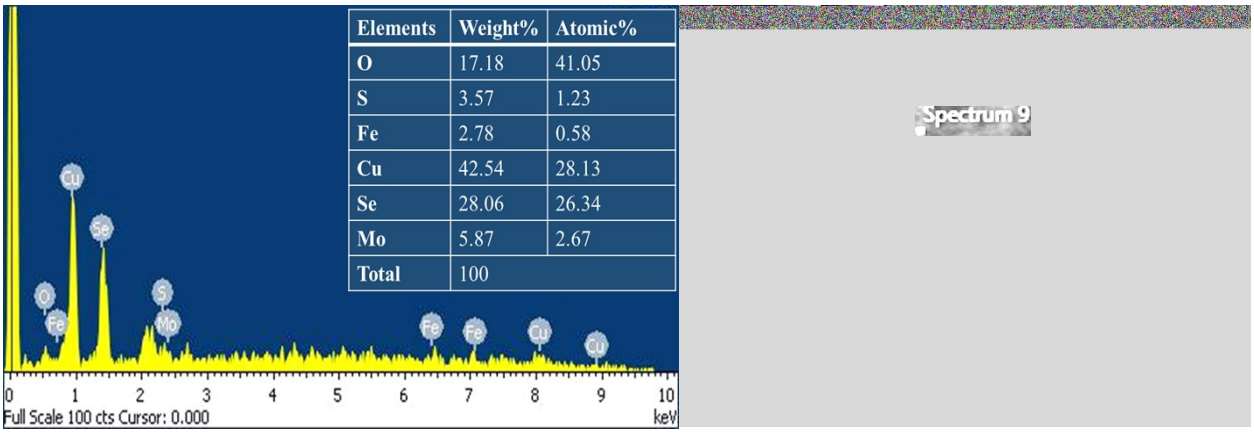

Figure S7. Small-area SEM-EDS compositional analyses of the $CuSe_2$ phase in the the $FeMoO_4/CuFe_2S_3/CuSe_2$ catalyst.

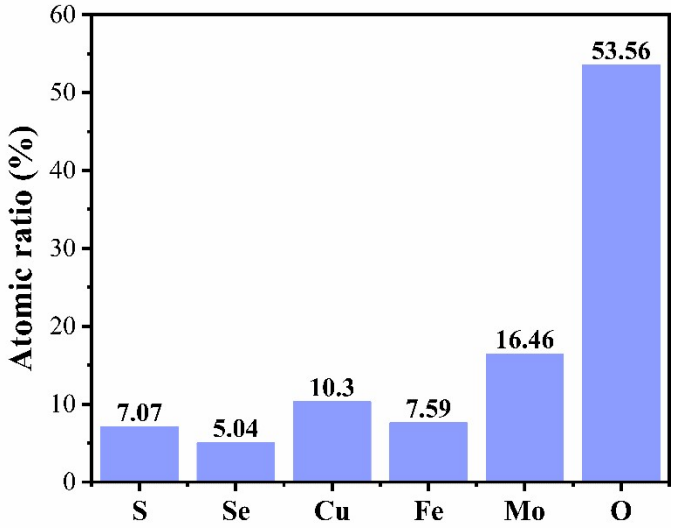

Figure S8. Atomic ratios of the $Fe(MoO_4)/CuFe_2S_3/CuSe_2$ tri-phase.

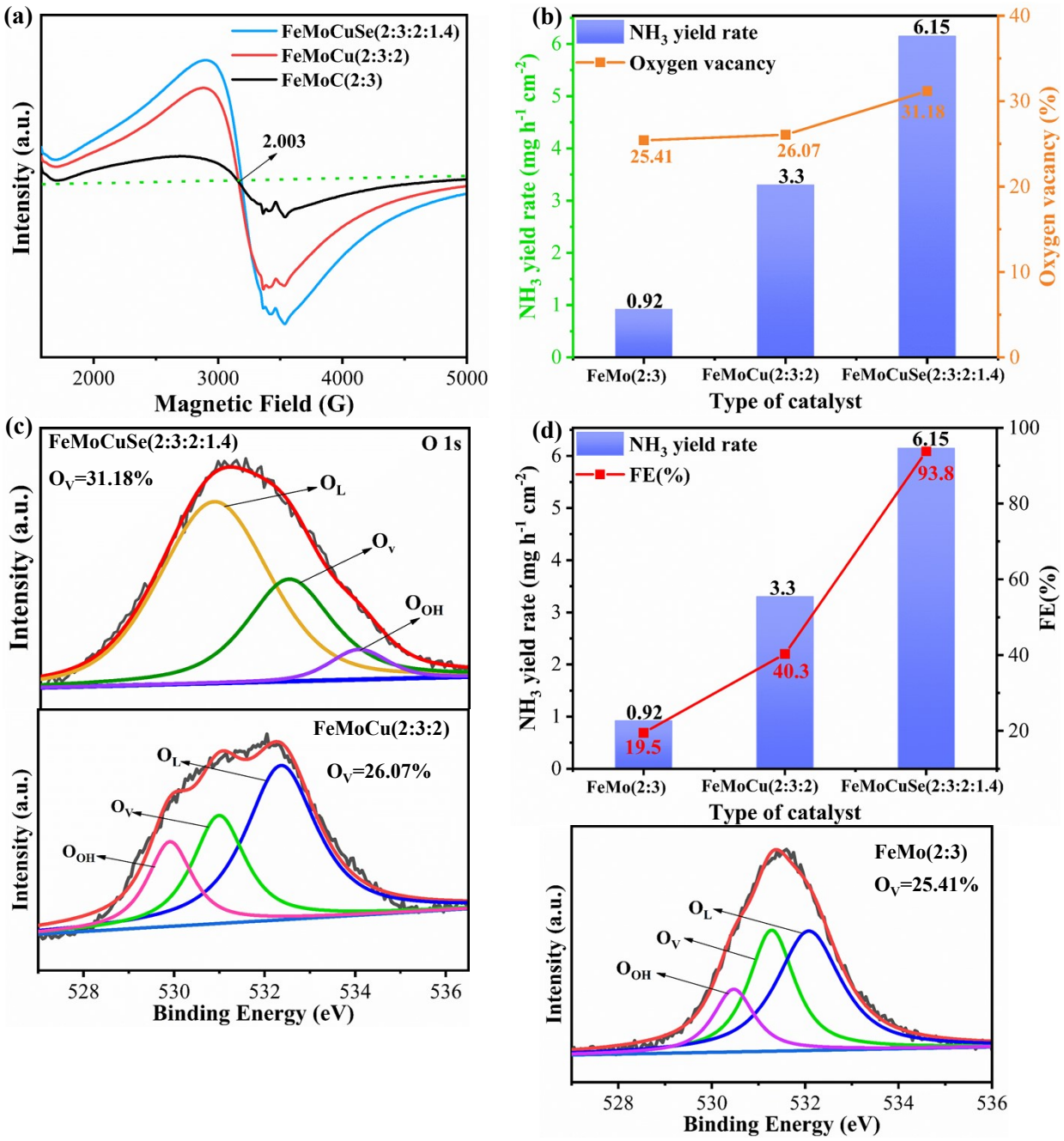

Figure S9. (a) EPR spectra of bimetal FeMo (2:3), FeMoCu (2:3:2), and FeMoCuSe (2:3:2:1.4) catalysts. (b) Quantitative comparison between oxygen vacancy and N_2RR performance of FeMo (2:3), FeMoCu (2:3:2), and FeMoCuSe (2:3:2:1.4). (c) Comparison of oxygen vacancy concentrations in FeMo (2:3), FeMoCu (2:3:2), and FeMoCuSe (2:3:2:1.4). (d) NH_3 yields for FeMo (2:3), FeMoCu (2:3:2), and FeMoCuSe (2:3:2:1.4) catalysts for a 2 h test.

Table S2. ICP-MS elemental analyses in $FeMoO_4/CuFe_2S_3/CuSe_2$ catalyst.

Element	Atomic %	RSD (%)
Fe	18.69	0.25%
Mo	27.10	0.25%
Cu	25.89	0.54%
Se	15.17	0.39%
S	13.15	-

Table S3. XPS atomic concentration of Fe, Mo, Cu, Se, S, and O in the $FeMoO_4/CuFe_2S_3/CuSe_2$ electrocatalysts, obtained from the Fe 2p, Mo 3d, Cu 2p, Se 3d, S 2p, and O 1s spectra, respectively.

Catalyst	Element	Peak area (%)		
$FeMoO_4/CuFe_2S_3/CuSe_2$	Fe	3.96	Fe^{3+}	59.9%
			Fe^{2+}	40.1%
	S	4.87	S^{2-}	100%
	Mo	8.59	Mo^{4+}	66%
			Mo^{6+}	34%
	Cu	6.14	Cu^{2+}	100%
	Se	5.95	Se^{2-}	100%
	O	70.48	O_L	63.16%
			O_V	31.18%
			O_H	5.64%

$$\%Mo = \left(\frac{peak\ area\ of \frac{Mo}{ASF}}{Peak\ area\ of \frac{Mo}{ASF} + paek\ area\ of \frac{Fe}{ASF} + Peak\ area\ of \frac{Cu}{ASF} + peak\ area\ of \frac{O}{ASF} + peak\ area\ o} \right) \times 100$$

%

Table S4. Calculation of elemental composition by EDS analysis of $FeMoO_4/CuFe_2S_3/CuSe_2$ combined with the XPS data.

EDS from point area	Fe	Mo	O	Cu	Se	S
The $CuFe_2S_3$ phase		Combining the Cu and Fe valence states and the data from the bulk $CuFe_2S_3$ cubic-like nanostructures with the basis of valence charge balance for an ionic compound. The elemental composition for the cube-like crystals, as determined by analysis (**Figure S6**), revealed 28.68% Cu, 22.63% Fe, 25.38% O, 20.63% S, and trace amounts of Se and Mo. The $CuFe_2S_3$ phase can be viewed: $\rightarrow Cu_{28.68}^{2+}(Fe_{0.40}^{2+}Fe_{0.60}^{3+})_{28.68}(O_{25.38}S_{20.63})$ ---Valence charge balance $\rightarrow 28.68\ Cu_1^{2+}(Fe_{0.4}^{2+}Fe_{0.6}^{3+})_{1.39}(O_{1.23}S_{1.64})$ $\rightarrow 28.68 Cu_1^{2+}(Fe_{0.4}^{2+}\square_{0.3}Fe_{0.6}^{3+})_{1.39}(O,S)_3$--Charge balance of defects $\rightarrow 28.68\ Cu_1^{2+}(Fe_{0.308}^{2+}\square_{0.231}Fe_{0.462}^{3+})_{1.39}(O_{0.773}S_{0.227})_3$ $\rightarrow 28.68\ Cu_1^{2+}(Fe_{0.308}^{2+}\square_{0.231}Fe_{0.462}^{3+})_{2\text{-}1.39}(O_{0.773}S_{0.227})_3$ $\rightarrow 28.68_{CuFe_{2-x}(O,S)_3}$				
	Theoretical	$CuFe_2S_3 = CuS{\cdot}2FeS$				
	Defects	$Fe^{3+}\_to\_Fe^{2+}$ defect (Fe_{Fe}^{1+}); Fe^{2+} vacancy $\left(V_{Fe}^{2-}\right)$				
30.5% iron vacancies in $CuFe_{2-x}S_3$						
The $FeMoO_4$ phase		For the smaller rod-like crystals (**Figure S5**), the components have 13.26% Fe, with 40.05% Fe^{2+} and 59.9% Fe^{3+}, and 20.65% Mo, with 66% Mo^{4+} and 33.99% Mo^{6+}. The $FeMoO_4$ phase can				

		be viewed as: $\rightarrow (Fe^{2+}_{0.401} Fe^{3+}_{0.599})_{13.26} [Mo^{4+}_{0.660} Mo^{6+}_{0.339}]_{20} O_{61.23}$ $\rightarrow 13.26\ (Fe^{2+}_{0.401} Fe^{3+}_{0.599}) [Mo^{4+}_{0.660} Mo^{6+}_{0.339}]_{1.5} O_{5.46}$ $\rightarrow 8.84\ (Fe^{2+}_{0.401} Fe^{3+}_{0.599})_{0.66} [Mo^{4+}_{0.660} Mo^{6+}_{0.339}]_{1} O_{3.07}$ $\rightarrow 8.84\ [(Fe^{2+}_{0.401} Fe^{3+}_{0.599})_{1-0.34} [Mo^{4+}_{0.55} Mo^{6+}_{0.45}]_{1} O_{4-0.93}$ $\rightarrow 8.84\ Fe_{1-x}(MoO_{4-y})$
	Theoretical	$FeMoO_4 = FeO \cdot MoO_3$
	Defects	Fe^{2+} vacancy $\left(V^{2-}_{Fe}\right)$; $Fe^{3+}\_to\_Fe^{2+}$ defect $\left(Fe^{1+}_{Fe}\right)$; $Mo^{4+}\_to\_Mo^{6+}$ defect $\left(Mo^{2-}_{Mo}\right)$
23.25% oxygen vacancies in $Fe_{1-x}MoO_{4-y}$		
The $CuSe_2$ phase		For the highly porous, or sponge-like crystals, the components have 28.13% Cu, and 26.34% Se. From Table S3, Se is in the form of Se^{2-} instead of a diselenide ion $(Se_2)^{2-}$, so overall neutrality can hold with Cu^{2+}: The $CuSe_2$ phase can be viewed as: $\rightarrow Cu^{2+}_{28.13} Se^{2-}_{26.34} = 28.13\ Cu^{2+}_{1}\ (Se^{2-}_{0.94})\ \sim\ 28.13\ Cu^{2+}_{1}\ (Se^{2-}_{1})$ $Cu^{2+}\ (Se^{2-}_{1.0})(V^{1+}_{Se})$
	Theoretical	$CuSe_2 = Cu^{2+}(Se_2)^{2-}$
	Defects	Se^{2-}-to-Se^{1-} defect (Se^{1-}_{Se}) Se^{1-} vacancy (V^{1+}_{Se})
50 % Se^{1-} vacancies in $CuSe_{2-z}$		

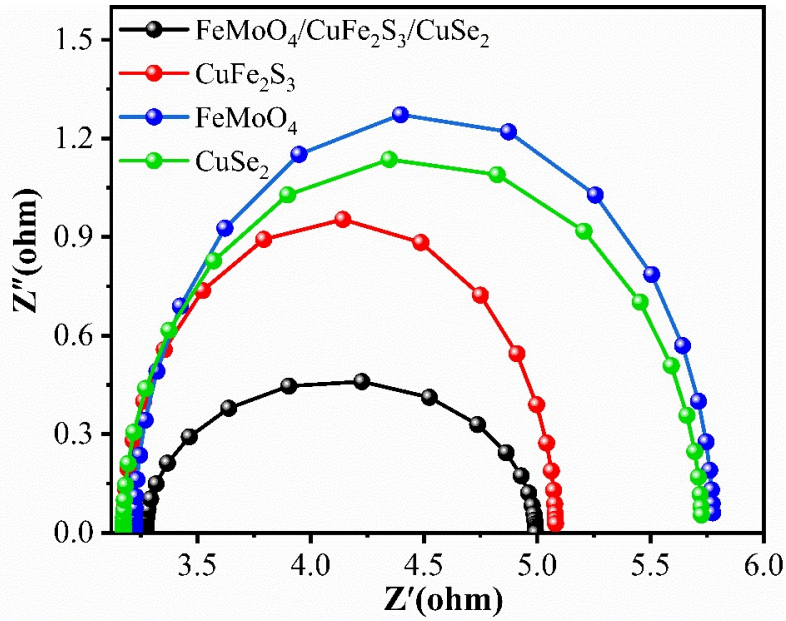

Figure S10. Nyquist plots comparing the electrochemical impedance behavior of $FeMoO_4$, $CuFe_2S_3$, $CuSe_2$, and the $FeMoO_4/CuFe_2S_3/CuSe_2$ electrocatalysts in an aqueous electrolyte containing 0.5 M Na_2SO_4.

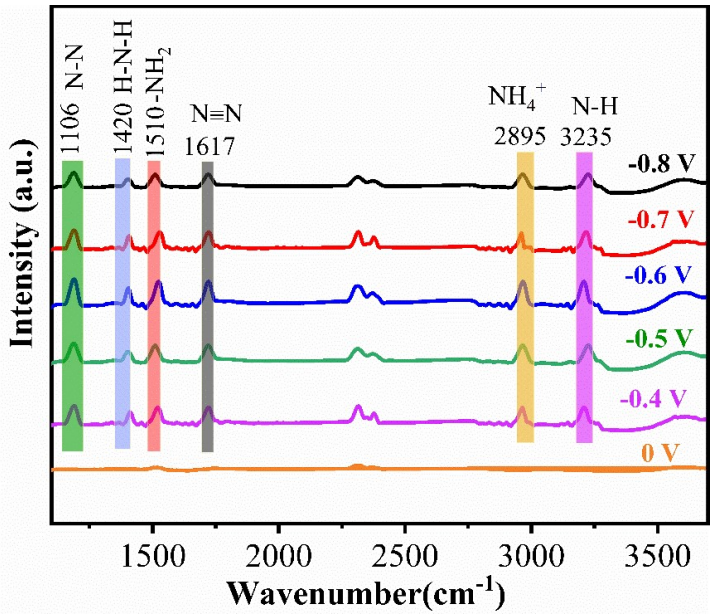

Figure S11. In situ FT-IR spectra of FeMoCuSe (2:3:2:1.4) recorded in 0.5 M Na_2SO_4 under cathodic polarization at potentials from −0.4 to −0.8 V vs. RHE.

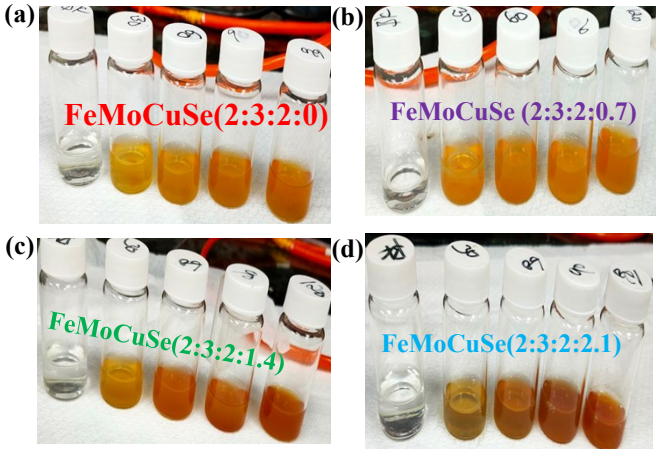

Figure S12. Changes in the color of solutions with the reaction time after adding Nessler reagent at 30 min intervals for (a) FeMoCuSe (2:3:2:0), (b) FeMoCuSe (2:3:2:0.7), (c) FeMoCuSe (2:3:2:1.4), and (d) FeMoCuSe (2:3:2:2.1).

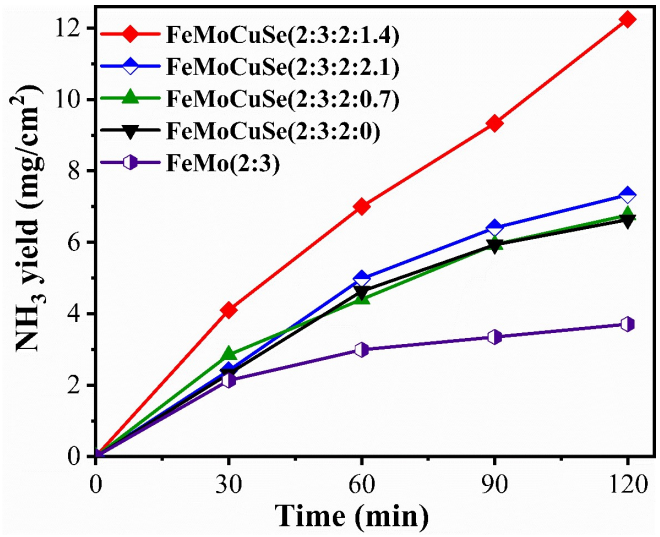

Figure S13. NH_3 yield data production at 30-minute intervals after adding Nessler reagent.

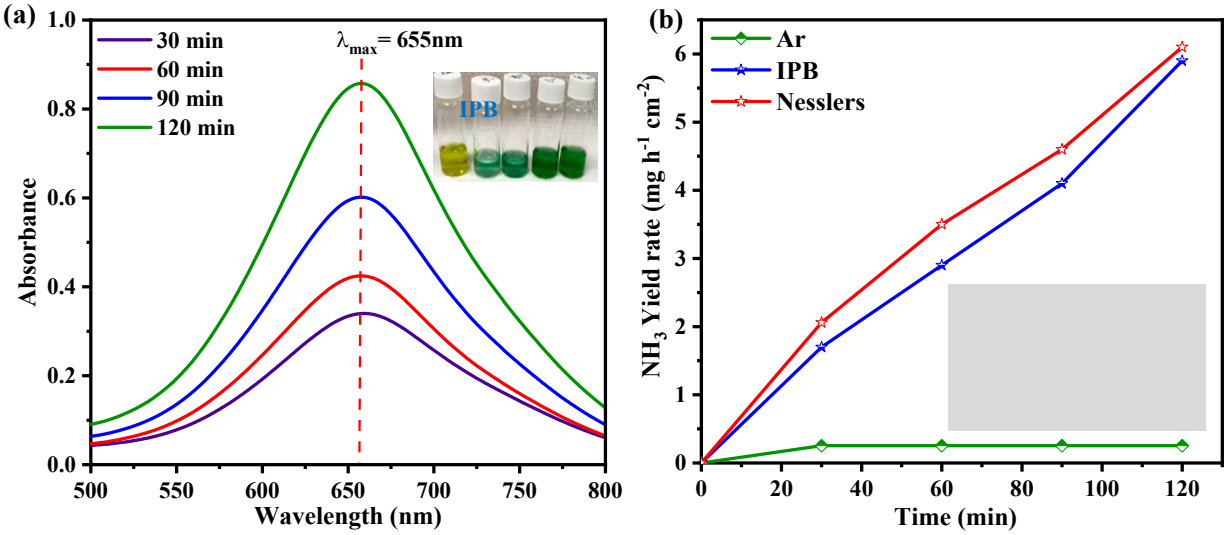

Figure S14. (a) UV-vis spectra of NH_3, confirmed by the Indophenol blue method, with 30 min interval electrolysis. (b) Comparison between Nessler and IPB methods for ammonia detection of FeMoCuSe (2:3:2:1.4) in 0.5M Na_2SO_4 at -0.6V vs. RHE.

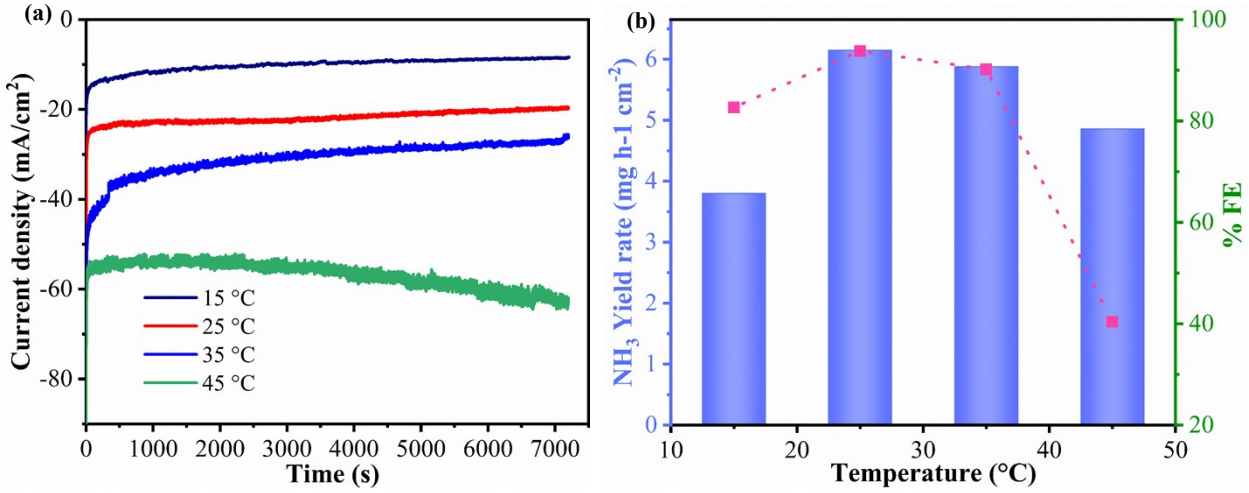

Figure S15. Influence of temperature on the electrocatalytic N_2 reduction reaction (N_2RR): (a) chronoamperometric responses at various temperatures, and (b) corresponding NH_3 yield rates and FE.

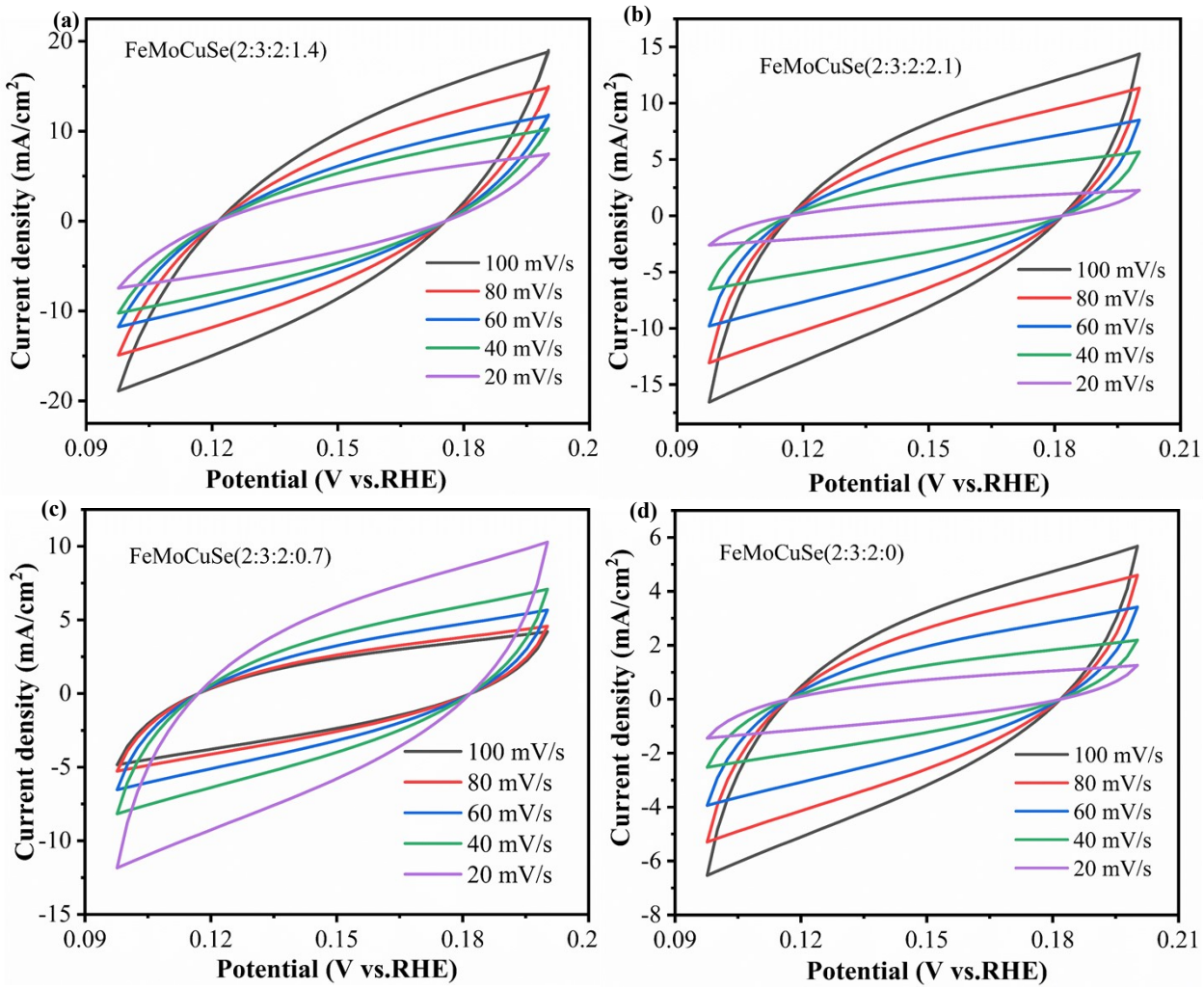

Figure S16. CV tests for (a) FeMoCuSe (2:3:2:1.4), (b) FeMoCuSe (2:3:2:2.1), (c) FeMoCuSe (2:3:2:0.7), and (d) FeMoCuSe (2:3:2:0).

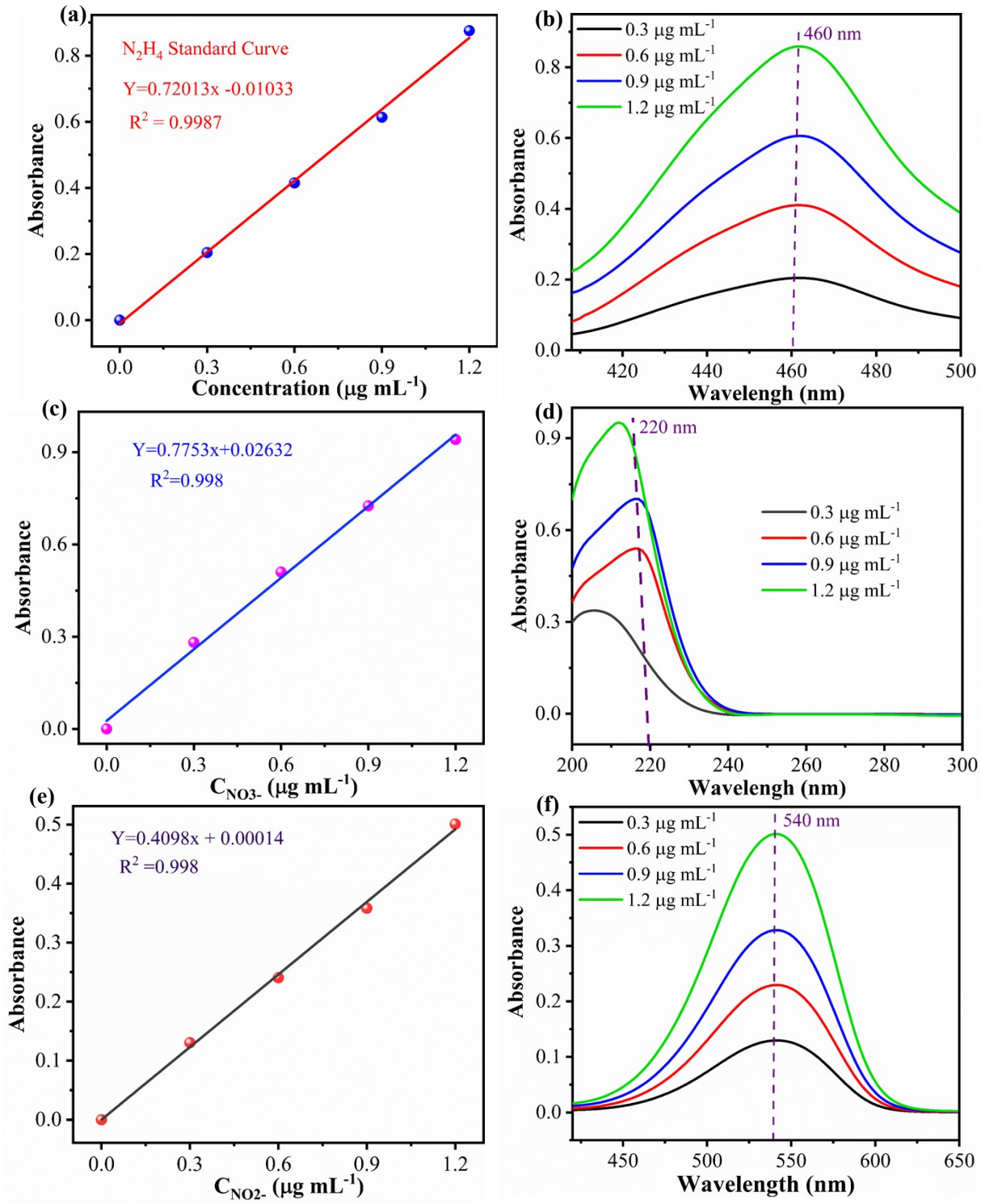

Figure S17. (a) UV–Vis absorption spectra of N_2H_4 solutions measured after 20 minutes of incubation at room temperature. (b) Calibration curve used to determine the N_2H_4 concentrations. (c) Calibration for NO_3^- quantification. (d) UV–Vis absorption spectra of $NaNO_3$ solutions with

known concentrations. (d) Calibration curve to show the relationship between $NaNO_3$ concentration and absorbance. (e) UV–Vis absorption spectra of $NaNO_2$ solutions with known concentrations. (f) Calibration curve depicting the relationship between $NaNO_2$ concentration and absorbance.

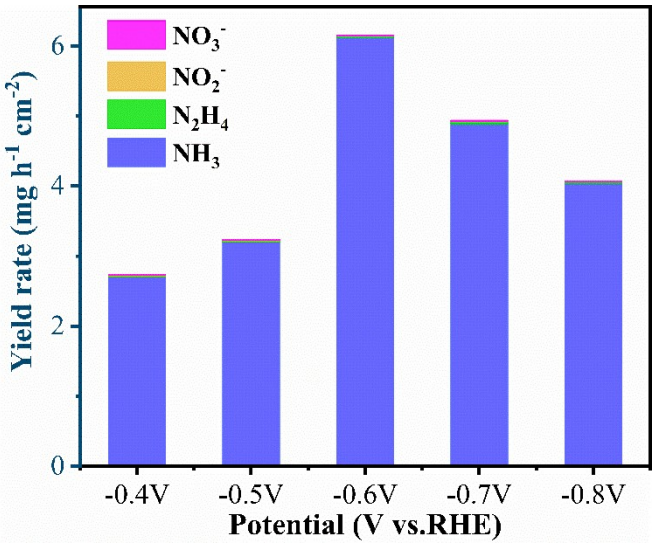

Figure S18. Yield rates of NH_3, NO_3^-, NO_2^-, and N_2H_4 produced by the FeMoCuSe (2:3:2:1.4) catalyst at different applied potentials after catalytic reaction for 2h in the cell system.

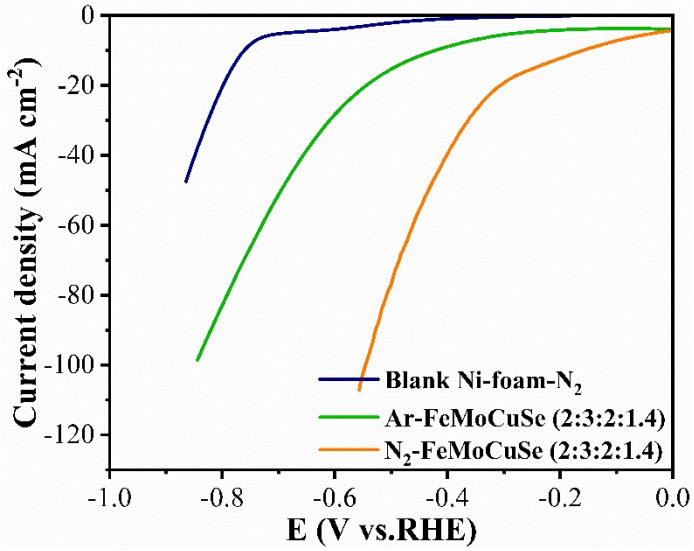

Figure S19. LSV curve comparison between blank Ni-foam (catalyst-free) and FeMoCuSe (2:3:2:1.4) in a N_2-saturated 0.5 M Na_2SO_4 electrolyte at −0.6 V vs. RHE.

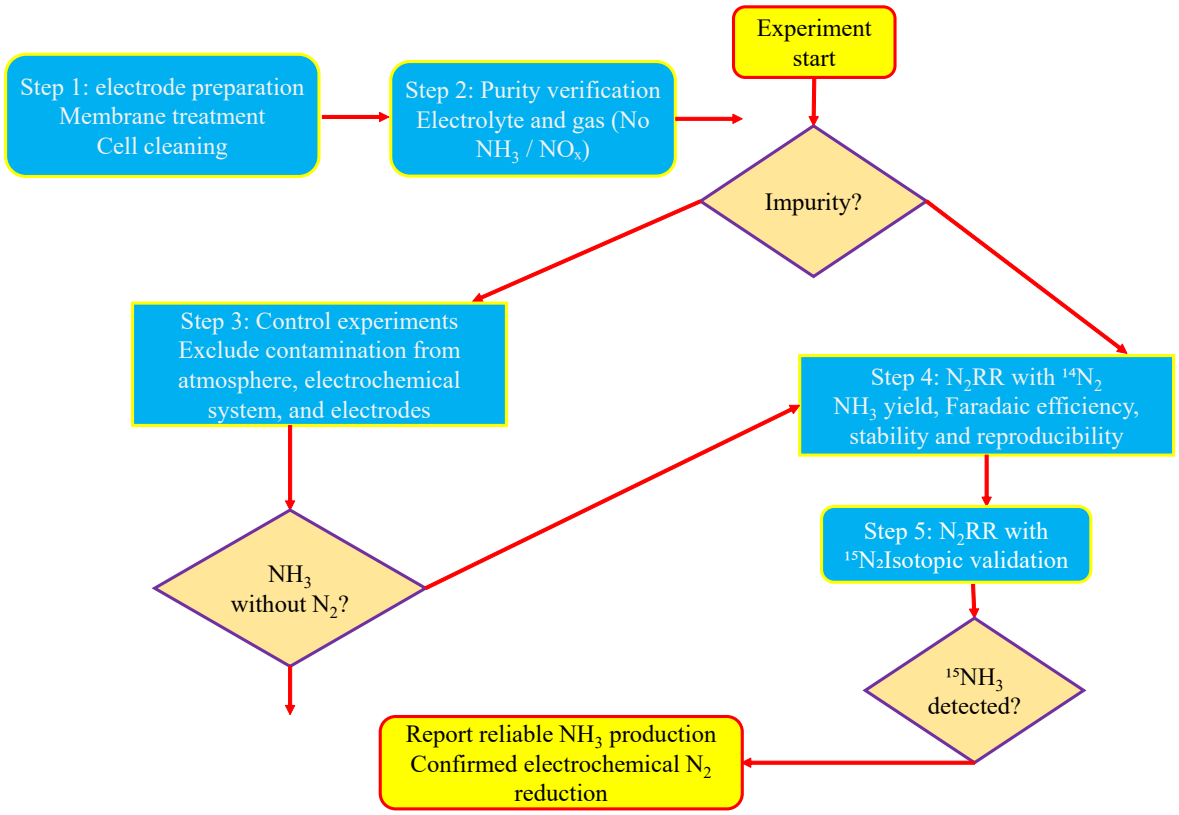

Figure S20. Experimental work flow used to reliably verify the nitrogen reduction reaction (N_2RR).

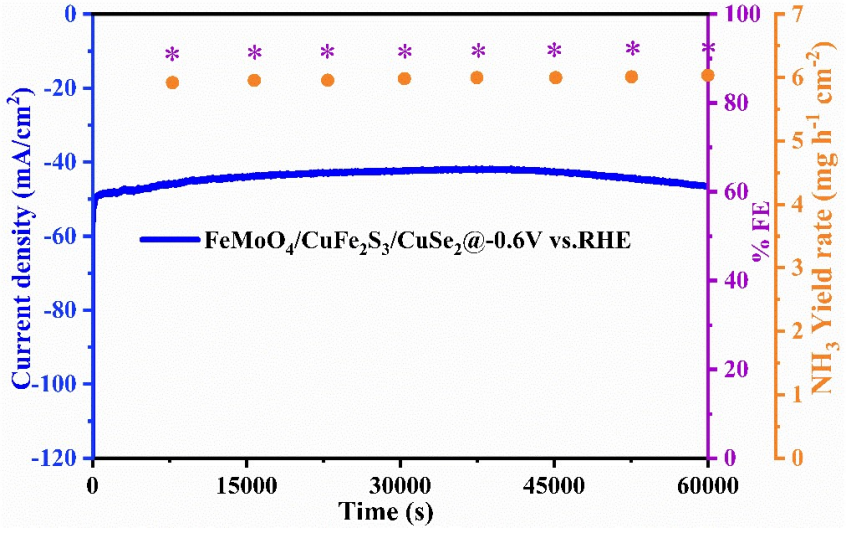

Figure S21. The catalysis curves for $FeMoO_4/CuFe_2S_3/CuSe_2$ in a N_2-saturated 0.5 M Na_2SO_4 electrolyte solution at -0.6 V vs. RHE over 16 hours in an H-cell.

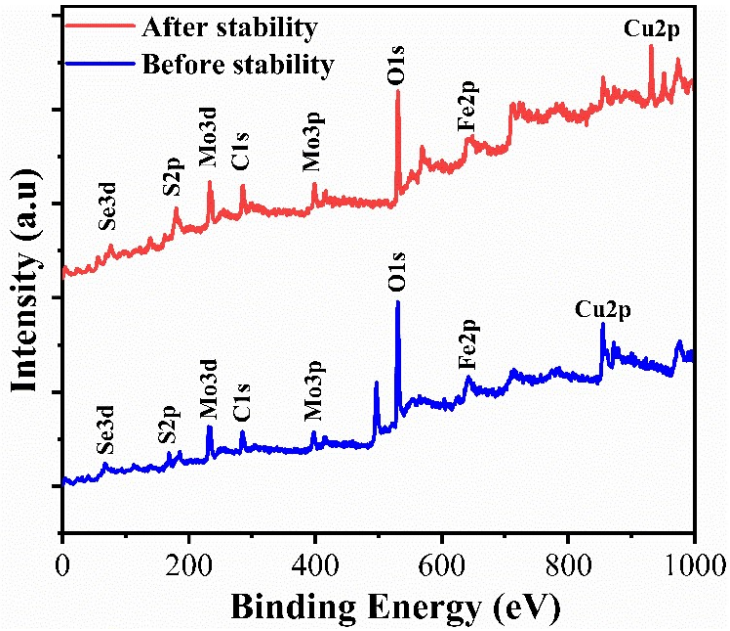

Figure S22. XPS survey spectrum of $FeMoO_4/CuFe_2S_3/CuSe_2$ before and after stability test.

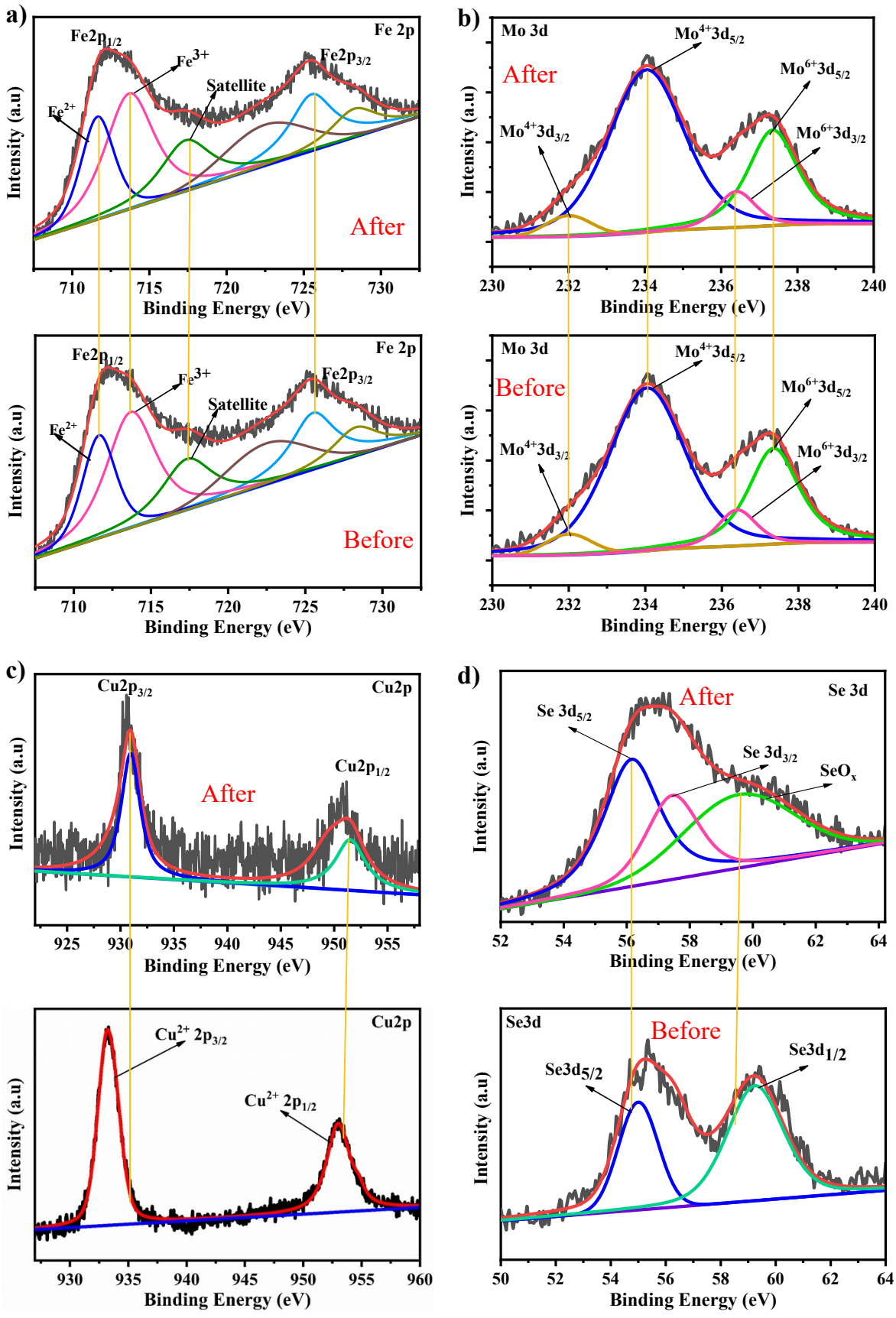
a)
Fe2p1/2
Fe3+
Satellite
Fe2p3/2
Fe2+
Fe 2p
After
Intensity (a.u)
710
715
720
725
730
Binding Energy (eV)
Fe2p1/2
Fe3+
Satellite
Fe2p3/2
Fe2+
Fe 2p
Before
Intensity (a.u)
710
715
720
725
730
Binding Energy (eV)
b)
Mo 3d
Mo4+3d5/2
After
Mo6+3d5/2
Mo4+3d3/2
Mo6+3d3/2
Intensity (a.u)
230
232
234
236
238
240
Binding Energy (eV)
Mo 3d
Mo4+3d5/2
Before
Mo6+3d5/2
Mo4+3d3/2
Mo6+3d3/2
Intensity (a.u)
230
232
234
236
238
240
Binding Energy (eV)
c)
Cu2p3/2
Cu2p
Cu2p1/2
After
Intensity (a.u)
925
930
935
940
945
950
955
Binding Energy (eV)
Cu2p
Cu2+ 2p3/2
Cu2+ 2p1/2
Intensity (a.u)
930
935
940
945
950
955
960
Binding Energy (eV)
d)
After
Se 3d
Se 3d5/2
Se 3d3/2
SeOx
Intensity (a.u)
52
54
56
58
60
62
64
Binding Energy (eV)
Se3d
Before
Se3d5/2
Se3d1/2
Intensity (a.u)
50
52
54
56
58
60
62
64
Binding Energy (eV)

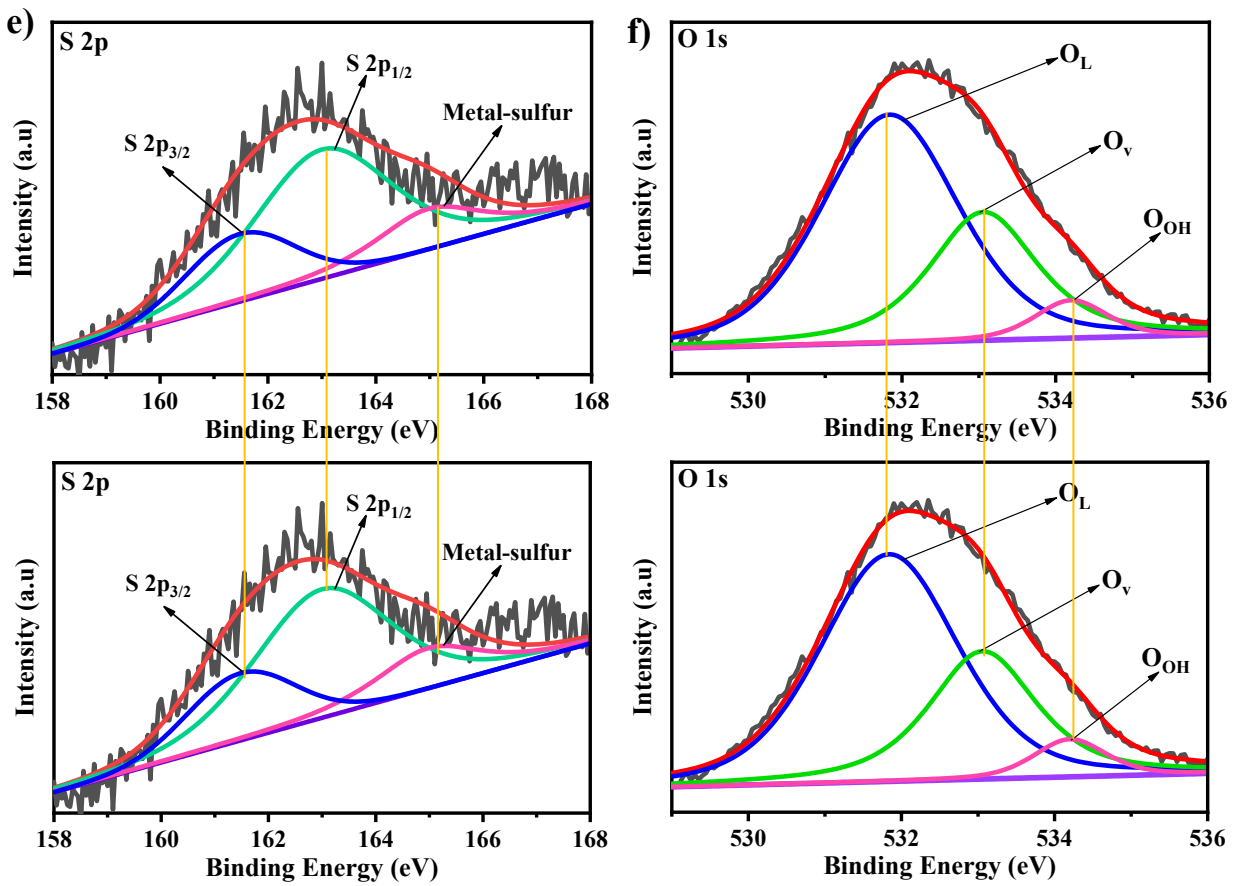

Figure S23. XPS spectra of (a) Fe 2p, (b) Mo 3d, (c) Cu 2p, (d) Se 3d, (e) S 2p, and (f) O 1s for the $FeMoO_4/CuFe_2S_3/CuSe_2$ catalyst before and after stability tests.

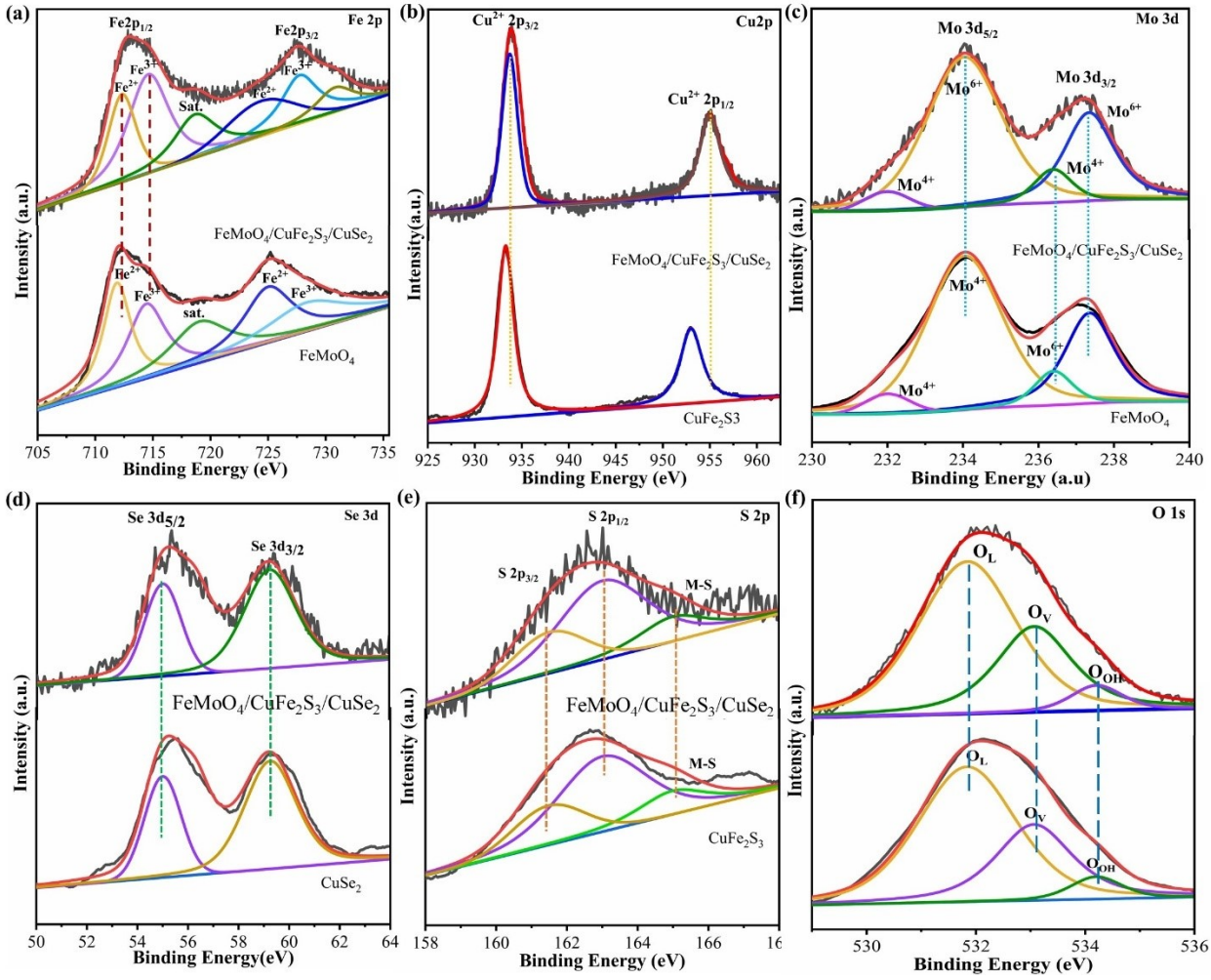

Figure S24. XPS analyses of $FeMoO_4$, $CuFe_2S_3$, and $CuSe_2$ alongside the $FeMoO_4/CuFe_2S_3/CuSe_2$ electrocatalyst, highlighting the differences in their surface chemical states.

Table S5. Comparison of the N_2RR activity for $FeMoO_4/CuFe_2S_3/CuSe_2$ with other recently reported catalysts.

No.	Catalyst	Synthesis method	Potential vs. RHE (V)	Electrolyte	NH_3 yield rate	FE (%)	Ref.
1	$FeMoO_4/CuFe_2S_3/CuSe_2$	Hydrothermal	−0.6	0.5M Na_2SO_4	6.15 mg h^{-1} cm^{-2}	93.8	This work
2	Bi_2MoO_6/Cu_8S_5	Hydrothermal	−0.6	0.5M Na_2SO_4	6.75 mg h^{-1} cm^{-2}	57.9	4
3	$Cu_2Mn_3O_8/CeS_2$	Hydrothermal	−0.689	0.5M Na_2SO_4	4.60 mg h^{-1} cm^{-2}	47.2	5
4	$Fe_2V_4O_{13}/Mo_2S_3$	Hydrothermal	-0.7	0.5M Na_2SO_4	5.46 mg h^{-1} cm^{-2}	47.6	6

5	$Cu_4Bi_5S_{10}/Mn_4V_2O_9$	Hydrothermal	−0.6	0.5M KOH	4.36 mg h^{-1} cm^{-2}	46.1	7
6	$(V, Ni, Mn)_3O_{4-x}/Nb_2O_{5-y}$	Hydrothermal	−0.5	0.1M Na_2SO_4	3.19 mg h^{-1} cm^{-2}	22.7	8
7	$(Fe,Mn,Ga)_3O_{4-x}/(Mn,Fe)_2O_{3-y}$	Hydrothermal	−0.6	0.1M Na_2SO_4	2.04 mg h^{-1} cm^{-2}	5.77	9
8	Cu_3BiS_3/MnO_2	Hydrothermal	−0.75	0.5M Na_2SO_4	3.60 mg h^{-1} cm^{-2}	31.4	10
9	CoFeB	Chemical reduction method	−0.2	0.05 M H_2SO_4	3.5×10^{-2} mg h^{-1} cm^{-2}	31.6	11
10	NiS_x/MoS_2	Hydrothermal	−0.60	0.1 M Na_2SO_4	3.43×10^{-2} mg h^{-1} cm^{-2}	48.53	12
11	Bi_2S_3/MoS_2	Hydrothermal	−0.40	0.1 M Na_2SO_4	5.46×10^{-2} mg h^{-1} cm^{-2}	58.56	13
12	$MoSe_2$	Chemical etching &CVD process	−0.3	0.1 M Na_2SO_4	6.16×10^{-3} mg h^{-1} cm^{-2}	37.82	14
13	(Vr-$ReSe_2$@CBC)	Combining hydrothermal, heat treatment	−0.25	0.1M Na_2SO_4	28.3 mg h^{-1} cm^{-2}	42.5	15
14	$TiO_2/Ag/Cu_7S_4$@Se	Electrodeposition	−0.20	0.1 M KOH	39.16 mg $h^{-1}cm^{-2}$	51.05	16
15	$FeCuS_x$	-	−0.1	0.1 M KOH.	1.37×10^{-2}mgh $^{1}cm^{-2}$	53.78	17
16	B_4C/CNTs	-	−0.6	0.1M Na_2SO_4	3.36×10^{-2}mgh $^{1}cm^{-2}$	78.2	18
17	B-$TiO_{1.8}$	Hydrothermal	−0.1	0.1 M Li_2SO_4	3.16×10^{-2} mgh $^{1}cm^{-2}$	47.7	19
18	V_{Pd}-$PdH_{0.41}$	Facile wet-chemical way	−0.05	0.1 M Li_2SO_4	6.58 mg h $^{1}cm^{-2}$	46.5	20

References

1. S. Z. Andersen, V. Čolić, S. Yang, J. A. Schwalbe, A. C. Nielander, J. M. McEnaney, K. Enemark-Rasmussen, J. G. Baker, A. R. Singh and B. A. Rohr, *Nature*, 2019, **570**, 504-508.
2. T. G. Eshetu, M. E. Ayalew, A. A. Mitiku, Q.-N. Ha, M. Z. Silitonga, V.-N. Tran and D.-H. Kuo, *Chemical Engineering Journal*, 2025, 171695.

3. Y. Cui, A. Dong, Y. Qu, J. Zhang, M. Zhao, Z. Wang and Q. Jiang, *Chemical Engineering Journal*, 2021, **426**, 131843.

4. A. A. Mitiku, M. E. Ayalew, T. G. Eshetu, Q.-N. Ha, X. Chen, M. Z. Silitonga, V.-N. Tran, L.-D. Tsai, Y.-W. Tsai and D.-H. Kuo, *Journal of Materials Chemistry A*, 2026.

5. A. A. Mitiku, M. H. Urgesa, Q.-N. Ha and D.-H. Kuo, *Journal of Alloys and Compounds*, 2025, 180006.

6. M. E. Ayalew, T. N. Gemeda, Q.-N. Ha, T. G. Eshetu and D.-H. Kuo, *Applied Catalysis B: Environment and Energy*, 2025, 125602.

7. M. H. Urgesa, Q.-N. Ha, K.-H. Lin, L.-D. Tsai, Y.-W. Tsai and D.-H. Kuo, *Journal of Materials Chemistry A*, 2025, **13**, 1355-1371.

8. T. N. Gemeda, D.-H. Kuo and Q.-N. Ha, *Green Chemistry*, 2023, **25**, 10498-10512.

9. T. N. Gemeda, D.-H. Kuo, G. Sisay Wolde and N. S. Gultom, *ACS Applied Energy Materials*, 2023, **6**, 8063-8071.

10. M. H. Urgesa, D.-H. Kuo, T. N. Gemeda, Q.-N. Ha and N. S. Gultom, *Applied Catalysis B: Environment and Energy*, 2024, **355**, 124194.

11. M. Arif, A. Kumar, M. A. Mushtaq, U. Azhar, M. Sagir, M. B. Tahir, U. Talib, S. Ajmal, K. M. Alotaibi and G. Yasin, *Chemical Engineering Journal*, 2023, **473**, 145368.

12. X. Chen, Y. Wang and X. Meng, *Chemical Engineering Journal*, 2024, **479**, 147701.

13. X. Chen, G. Ren, Y. Wang, Z. Li, Z. Zhang and X. Meng, *Applied Catalysis B: Environment and Energy*, 2024, **355**, 124173.

14. D. Chen, M. Luo, S. Ning, J. Lan, W. Peng, Y. R. Lu, T. S. Chan and Y. Tan, *Small*, 2022, **18**, 2104043.

15. F. Lai, W. Zong, G. He, Y. Xu, H. Huang, B. Weng, D. Rao, J. A. Martens, J. Hofkens and I. P. Parkin, *Angewandte Chemie International Edition*, 2020, **59**, 13320-13327.

16. L. Zhang, P.-Y. Liu, W.-Z. Chen, Y. Liu, Z. Liu and Y.-Q. Wang, *Inorganic Chemistry*, 2022, **61**, 7165-7172.

17. Y. Liu, L. Wang, L. Chen, H. Wang, A. R. Jadhav, T. Yang, Y. Wang, J. Zhang, A. Kumar and J. Lee, *Angewandte Chemie*, 2022, **134**, e202209555.

18. T. Li, H. Li, J. Wang, M. Zhang, Y. Zhang, T. Li, L. Shen, J. Bi and Y. Li, *ChemCatChem*, 2024, **16**, e202400115.

19. Y. Sun, Y. Han, X. Zhang, W. Cai, Y. Zhang, Y. Zhang, Z. Li, B. Li, J. Lai and L. Wang, *Applied Catalysis B: Environmental*, 2022, **319**, 121933.

20. Z. Wang, H. Zhao, J. Liu, D. Zhang, X. Wu, N. Nie, D. Wu, W. Xu, J. Lai and L. Wang, *Chemical Engineering Journal*, 2022, **450**, 137951.